Corrosion Science 99 (2015) 164–171

Contents lists available at ScienceDirect

Corrosion Science

journal homepage: www.elsevier.com/locate/corsci

SKPFM measured Volta potential correlated with strain localisation in microstructure to understand corrosion susceptibility of cold-rolled grade 2205 duplex stainless steel

C. Örnek*, D.L. Engelberg

Materials and Performance Centre & Corrosion and Protection Centre, School of Materials, The University of Manchester, Sackville Street, Manchester M13 9PL, United Kingdom

ARTICLE INFO

Article history:
Received 21 March 2015
Received in revised form 15 June 2015
Accepted 27 June 2015
Available online 23 July 2015

Keywords:
Duplex stainless steel
SKPFM
Cold rolling
Local misorientation
EBSD
Atmospheric corrosion

ABSTRACT

Scanning Kelvin probe force microscopy (SKPFM) of annealed and cold-rolled grade 2205 duplex stainless steel has been correlated with microstructure analysis using electron back-scattered diffraction (EBSD). In annealed microstructure Volta potential differences indicated micro-galvanic coupling between ferrite and austenite reasoning selective dissolution of ferrite. The introduction of cold work reduced the difference between both phases, but the development of local extremes in Volta potential was observed. Microstructure analysis revealed the presence of larger misorientation concentrations at these sites, which can explain the changes in observed corrosion behaviour, from selective dissolution in the annealed condition to localised corrosion attack after cold-rolling.

© 2015 The Authors. Published by Elsevier Ltd. This is an open access article under the CC BY license (http://creativecommons.org/licenses/by/4.0/).

1. Introduction

Duplex stainless steels (DSS) are frequently used for engineering applications, with complex shapes of components obtained via cold-rolling or shaping of plate and sheet material. Plastic deformation in polycrystalline material is generally heterogeneous, and leads to the development of misorientation variations and gradients in the microstructure, typically associated with strain localisation [1] . In duplex stainless steels, strain localisation is complex due to the mismatch of mechanical properties between body-centred-cubic ferrite (δ—bcc) and face-centred-cubic austenite (γ—fcc), which manifests itself during plastic deformation. Load sharing between both crystallographic phases is observed leading to heterogeneous deformation within the microstructure, with micro-yielding near grain boundaries in the ferrite, augmented by plastic deformation and dislocation pile-ups in the austenite [2,3]. Pitting corrosion [4,5] and crack nucleation [6] is often triggered at such sites, but cracks have also been observed to nucleate at slip bands due to the presence of local differences in elastic anisotropy [7].

The magnitude of misorientation within grains increases with the introduction of plastic strain, which is often used as a quantitative measure to describe the degree of microstructure deformation [1]. However, the introduction of plastic strain can also result in sub-structure formation associated with the re- arrangement of dislocations. Free dislocations generated during plastic deformation can readily re-arrange themselves, leading to the development of low-angle grain boundaries (LAGB) [1,8,9]. Plastic deformation results in an increase of the dislocation density which also affects local surface work function and hence the electrochemical potential [10]. The Electron Work Function (EWF) reflects the electron activity [10,11] and is the minimum energy required to remove electrons from inside a metal to a position far away from the surface on the atomic scale, but still close to the metal to be influenced by ambient electric fields [10–17]. It is not a material property but characteristic of the surface and is sensitive to pre-existing deformation, surface oxide layers, roughness, temperature, and adsorbents [15,17,18] . The EWF has been reported to decay with the induction of plastic deformation up to about 40% plastic strain after saturation is reached which was observed to be independent from the type of the material and was enhanced by the rate of deformation [10] . An increase of plastic strain and strain rate decreased the EWF hence the change in EWF could be attributed to the dislocation density in the microstructure. Furthermore, it was demonstrated that at grain boundaries the EWF decreased, in contrast to the grain inte-

* Corresponding author.
E-mail addresses: cem.oernek@manchester.ac.uk, cem_oernek@hotmail.de (C. Örnek), dirk.engelberg@manchester.ac.uk (D.L. Engelberg).

http://dx.doi.org/10.1016/j.corsci.2015.06.035
0010-938X/© 2015 The Authors. Published by Elsevier Ltd. This is an open access article under the CC BY license (http://creativecommons.org/licenses/by/4.0/).

rior of nanostructure materials, indicating that at such sites the electron activity is high with the result that the surface became more electrochemically reactive [11] . Such an increase in electrochemical reactivity affects local and overall corrosion performance of the material [11].

The related Volta potential (Ψ) is the potential difference between a position infinitely far away from the surface and a position just outside the surface, and is the measureable quantity characterising electrochemical behaviour of a metal [12,17]. The scanning Kelvin probe force microscopy (SKPFM) technique allows detection of local EWF (if the EWF of the tip is known), or Volta potential differences ($\Delta\Psi$) between an atomic force microscopy tip (usually Pt coated) and the metal surface [14,15,19]. The lateral resolution of SKPFM can be as high as 10's of nm in ambient air, with a sensitivity up to 10–20 meV [19]. Volta potential is a characteristic property of a metal surface and can be used to understand electrochemical processes [16] . It is sensitive to any kind of surface defects, chemical variations, and residual stress [13,17]. Volta potential differences in microstructure have been used to predict corrosion behaviour [10,15,18,20–22]. Regions with larger ($\Delta\Psi$) indicate increased surface reactivity [11,15,18], and even a correlation between Volta potential differences measured in nominally dry air and their free corrosion potential (E_{corr}) pre-determined under immersed conditions has been reported [18].

Furthermore, a relationship between E_{corr} measured under thin electrolyte and the Volta potential difference was demonstrated [23]. Linear correlation of Volta potential measured via the Kelvin probe technique measured in air with the free corrosion behaviour (E_{corr}) upon immersed specimens [24], and this relationship was demonstrated to hold true for potentials measured via SKPFM [23] . However, SKPFM Volta potential differences in air may not always correlate with corrosion potentials measured in aqueous solution, and interpretation of SKPFM data regarding corrosion phenomena need to be treated with caution [15]. This shortfall can be minimised by conducting SKPFM measurements in humid air (>60% relative humidity), where several mono-layers of water are present on the metal surface, mimicking "solution- like" behaviour [25].

The purpose of the work reported in this study was to investigate the effect of plastic deformation on local microstructure Volta potential differences ($\Delta\Psi$) and compare these results with atmospheric corrosion observations. The idea is that through the introduction of plastic deformation steep gradients of $\Delta\Psi$ on confined regions can be formed in the microstructure which may correlate with local strain heterogeneities and act as susceptible sites for localised corrosion and also for stress corrosion cracking. A duplex microstructure was chosen to maximise the effect of plastic strain on microstructure behaviour. Grade 2205 duplex stainless steel is considered by the UK's nuclear industry as a candidate container material for storage of intermediate-level radioactive waste (ILW) which undergoes various deformations [26]. Localised corrosion and, in particular, environment-assisted cracking has been considered as the main material degradation concern that may limit the integrity of ILW containers, which mechanistic understanding is required to support container lifetime predictions.

2. Experimental

A solution-annealed (mill annealed) grade 2205 DSS plate with a composition (in wt.-%) of 22.4Cr, 5.8Ni, 3.2Mo, 1.5Mn, 0.4Si, 0.016C, 0.18N, and Fe (bal.) was used in this study. The chemical composition of ferrite and austenite was determined by energy dispersive X-ray (EDX) technique interfaced to a scanning electron microscopy (SEM) as 25.0Cr, 4.3Ni, 4.3Mo, 1.7Mn, 0.5Si, and Fe (normalised) for ferrite, and 22.1Cr, 6.9Ni, 2.6Mo, 1.9Mn, 0.4Si, and Fe (normalised) for austenite, all in wt.-%. Cold rolling of the plate was performed with a thickness reduction of 40%, and rectangular coupon specimens ($8 \times 8 \times 8\ mm^3$) were cut from both the as-received and cold-rolled material. The surface of these coupons was prepared by grinding to 4000-grit, followed by mirror-finish polishing using 3, 1, ¼, and 0.1 μm diamond paste, and finalised with an OP-S polishing treatment.

Electron Back-Scattered Diffraction (EBSD) was used for material characterisation, by extracting grain size, crystallographic phase fraction, and local misorientation (LMO), with the latter indicative of the distribution of plastic strain in the microstructure. A FEI Quanta 650 scanning electron microscope (SEM) interfaced with a Nordlys EBSD detector from Oxford Instruments with Aztec V2.2 software was used for data acquisition. A step size of 0.15 μm over an area of $856 \times 746\ \mu m^2$ with an accelerating voltage of 20 kV was used for data acquisition. Data post processing was carried out with HKL Channel 5 software. High-Angle Grain Boundaries (HAGB's) were defined with misorientation ≥15° and Low Angle Grain Boundaries (LAGB's) between >1° and <15°. The grain size was determined by the mean linear intercept method as the mean of vertical and horizontal directions (twins disregarded). LMO maps were generated by using a 3×3 binning and a 5° threshold for the sub-grain angle threshold. This analysis gives the average LMO for a misorientation below the pre-determined sub-grain angle threshold, and this method was used to locate regions with higher concentrations of misorientation in the microstructure. The latter is typically associated with local micro-deformation in the form of plastic strain, due to the presence of dislocations [1].

All SKPFM measurements were performed prior to EBSD analysis of the same area to allow correlation of the results. A MultiMode 8 atomic force microscope from Veeco Instruments (AFM) with Nanoscope V8.15 acquisition programme from Bruker was used. OSCM-PT probe was employed for Volta potential ($\Delta\Psi$) measurements. The interleave lift height was 50 nm. The SKPFM scan size was $50 \times 50\ \mu m^2$ for the mill-annealed and $55 \times 55\ \mu m^2$ for the 40% cold-rolled sample. The tip was biased in order to zero the contact potential difference; therefore, positive potential differences measured indicate larger electronic activity of the microstructure. The reliability of the probe used was assessed by measuring the Volta potential difference of high quality HOPG (Highly Oriented Pyrolytic Graphite) which is the highest-quality synthetic form of graphite and commonly used to calibrate AFM probes [27]. Maximum potential differences of 1–2 mV were measured indicating good quality of the tip and maximum sensitivity of the system. The potential difference measured prior to and after the test was identical supporting the stability of the tip.

SKPFM tests were carried out in ambient air at a temperature of 30 °C with 38 ± 1% Relative Humidity (RH) or in a controlled environment of 33 ± 1 °C and 86 ± 1% RH. These humidity values were chosen to obtain information about the effect of water multi-layer coverage on Volta-potential differences, invoking "solution-like" behaviour [25]. The humidity was controlled in a sealed AFM chamber. Air was bubbled through a 5 l flask containing 5 M NaCl solution, heated by a water bath to 60 °C, creating a humid gas atmosphere which was directed to the chamber (a Perspex enclosure) housing the entire AFM setup. According to *Leygraf* et al. [25], at least six to ten monolayers of water with chloride species should form at 86% RH supporting a correlation of Volta potential measurements with local electrochemical activity. Temperature and relative humidity (RH) were recorded during the measurement with an EL-USB-2-LCD temperature and humidity data logger.

SKPFM data analysis was performed with the software NanoScope Analysis 1.5. Topography maps were flattened using 1st order flattening. Data acquisition was carried out with 512×512 pixel resolution, with all values reported relative to the work function of the AFM tip (Pt-tip). Potentials measured with higher and lower values with respect to the AFM tip indicate a net anodic and

net cathodic activity, respectively. Large Volta potential differences measured with respect to Pt mean lower absolute Volta potentials of the measured region/feature in the microstructure and, hence, higher corrosion activity. Volta potential maps of cold-rolled specimen measured in 86% RH environment were flattened and inverted in order to enhance potential contrast of local potential "hot-spots". Higher and lower potential values indicate net cathodic and net anodic activity, respectively, in this case only.

Atmospheric corrosion tests were performed on 4000-grit surface finished coupons. Tests were performed by exposing samples to 80 °C and 27% RH for 212 hrs. Water droplets containing $MgCl_2$ were applied onto the surface, yielding chloride deposition densities ranging from 145 μg/cm^2 to 1450 μg/cm^2. An Eppendorf micropipette was used to dispense the liquid with the volume of the droplet 0.5 μl producing an overall droplet radius of 1.7 mm (the effect of secondary spreading of the droplet was not considered). This exposure regime is close to the deliquescence point of $MgCl_2$, resulting in a concentrated, very aggressive $MgCl_2$ solution. Post exposure, the corrosion morphology was analysed with a Keyence VHX-200 optical microscope and the FEI Quanta 650 SEM. To identify whether the ferrite or the austenite phase had corroded, the mill-annealed sample was additionally etched in aqueous 40 wt.-% KOH solution, using 5 V for 5 s. This electrolytic etch stains the ferrite [28]. The cold-rolled specimen was analysed in the SEM in the backscattered electron imaging mode, to distinguish between ferrite and austenite.

3. Results and discussion

To demonstrate the effect of cold-rolling on microstructure development, EBSD phase maps of all three process orientations (ND, RD, and TD) of the annealed and 40% cold-rolled microstructures are shown in Fig. 1. Cold-rolling induced changes in grain shape and grain morphology, particularly in the austenite. The average grain size of ferrite as a sum of all process directions decreased from 7.3 ± 0.3 μm in the annealed condition to 5.1 ± 1.9 μm after 40% deformation, whilst the austenite grain size decreased from 7.1 ± 0.9 μm to 4.2 ± 1.3 μm. The average aspect ratio (vertical to horizontal mean length) in all process directions decreased from 1.8 to 1.2 in ferrite, and from 1.6 to 1.1 in austenite. This decrease in grain size can possibly be attributed to severely deformed and broken-up grains after cold deformation.

Other phases such as sigma (σ) or chi (χ) phase were not present in the microstructure. The austenite to ferrite phase ratio as an average of all three processing orientations was 44:56 and 47:53 for the solution annealed and 40% cold-rolled condition, respectively. The small increase in ferrite content with cold rolling is within typical microstructure variations observed in duplex stainless steel. There are also reports about the formation of deformation-induced bcc-martensite in duplex stainless steels, which would be co- indexed as ferrite since the Kikuchi patterns of martensite overlap with the Kikuchi patterns of ferrite in EBSD analysis. The martensite is typically needle-shaped and forms within the austenitic phase [29]. However, EBSD analysis of the 40% cold-rolled sample in Fig. 1 did not show any needle-shaped features.

Topography and Volta potential maps in air (38% RH) of the annealed sample with corresponding EBSD phase and LMO maps of the same region are shown in Fig. 2. The topography and Volta potential maps showed good correlation with the EBSD phase map, facilitating observation of both crystallographic phases to the corresponding ΔΨ values. Austenite and ferrite had distinctively different potential values, with ferrite showing higher potential values than austenite, meaning expected higher electrochemical activity. Mean ΔΨ values of 408 ± 16 mV and 320 ± 11 mV were measured for ferrite and austenite, respectively. The mean potential difference between both phases is about 70–90 mV, with steep potential gradients across interphases. Similar potential differences of 50–60 mV between ferrite and austenite, with ferrite indicating the less noble phase (anode) and austenite the nobler phase (cathode) has been reported by Sathirachinda et al. who investigated solution-annealed and sensitised microstructure and correlated local elemental depletion with local ΔΨ assessments [30]. The probe used was SCM-PIT with Pt-Ir coating and slightly different to that used in this study (OSCM-Pt probe with Pt coating). Small differences in chemical compositions and heat treatment history may also have contributed to different potentials measured. However, similar interphase potential gradients to our study were measured.

The potential variation within each phase is small (Fig. 2b), and no obvious potential hot-spots (individual sites with high local ΔΨ at confined regions) are detected. This indicates existence of a driving force for galvanic interaction between both phases, with expected onset of electrochemical activity at interphase boundaries and dissolution towards the ferrite. Differences in ΔΨ generally indicate a driving force for galvanic interaction, whereas local potential hot-spots or regions with steep potential changes (gradients) indicate susceptible sites for localised corrosion [31]. Selective corrosion attack in duplex stainless steel has frequently been observed on ferrite to occur in mild chloride-bearing environments, with nucleation at or in the vicinity of ferrite-austenite interphase boundaries, whilst austenite showed less corrosion and stress corrosion cracking susceptibility [32–41]. The corrosion potential (E_{corr}) of austenite in chloride media is lower than that of ferrite despite its lower chromium and molybdenum content. Preferred nitrogen and nickel partitioning in the austenite renders enhanced passivation behaviour and, hence, electrochemical nobility in chloride environments [38,39,42,43].

These data are in close agreement with the studies conducted by Sathirachinda et al. who also observed smooth potential distribution in the solution-annealed microstructure which seemed to have disrupted after sensitisation treatments showing local Volta potential extremes associated with enhanced susceptibility to localised corrosion which was confirmed by corrosion immersion tests using aggressive acidic chloride electrolyte [30]. The ferrite phase was seen to corrode primarily while the austenite seemed to remain unaffected which clearly demonstrated the galvanic interaction between ferrite and austenite where ferrite formed the net anode and austenite the net cathode [30].

The LMO map (Fig. 2d) indicates strain localisation mainly concentrated within ferrite and at small grain clusters with both ferritic and austenitic grains. The mean LMO has a maximum value of 2°, confirming the presence of only small local strain variations. LMO was similar in both phases, meaning that selective attack cannot be associated with LMO values.

The topography and corresponding Volta potential maps for the 40% cold-rolled condition in air (38% RH) are shown in Fig. 3. The mean potential of the entire region showed an overall ΔΨ rise of 170–190 mV with respect to the annealed microstructure condition. This large potential shift is expected to also result in a more corrosion susceptible microstructure (less noble). The driving force for a corrosion attack seemed to have increased after cold rolling possibly due to a strain-induced alteration in the electron band structure of the passive oxide layer caused by an enhancement of defects such as dislocation density (and other defects), where the amount of LAGB's and HAGB's increased. Lower work functions can result from defect-induced alteration in the electron band structure of passive oxide layers due to shifts in the Fermi level position caused by a change in the electron band gap of the oxide [44]. It has been shown in literature that the passivating layer is typically weakened by the introduction of large amounts of cold deformation, so that the corrosion current density and passive current density significantly increases

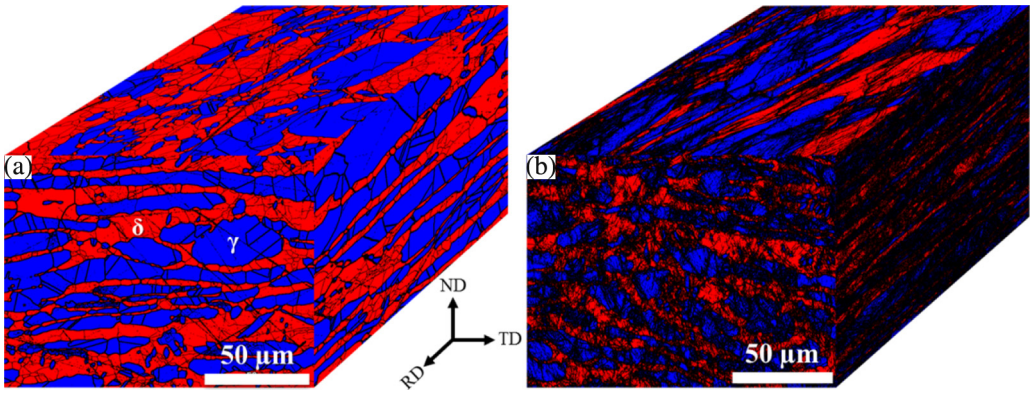

Fig. 1. EBSD phase maps of (a) annealed microstructure and (b) after 40% cold-rolling, with austenite shown in blue and ferrite in red. The thick black lines are HAGB's and thin lines LAGB's. (For interpretation of the references to colour in this figure legend, the reader is referred to the web version of this article.)

upon immersion in chloride containing media [45]. It is likely that dislocation multiplication in the microstructure induced by cold deformation can affect the passivating characteristics of both crystallographic phases, which in turn resulted in an increase of the mean $\Delta\Psi$ in the duplex microstructure. Since the Volta potential depends strongly on the electronic structure of the surface oxide layer of the metal (and other adsorbents) and due to the fact that substantially larger $\Delta\Psi$ was measured, the reduction of the practical nobility of the cold-rolled microstructure must be related to defect-caused degradation of the surface oxide layer

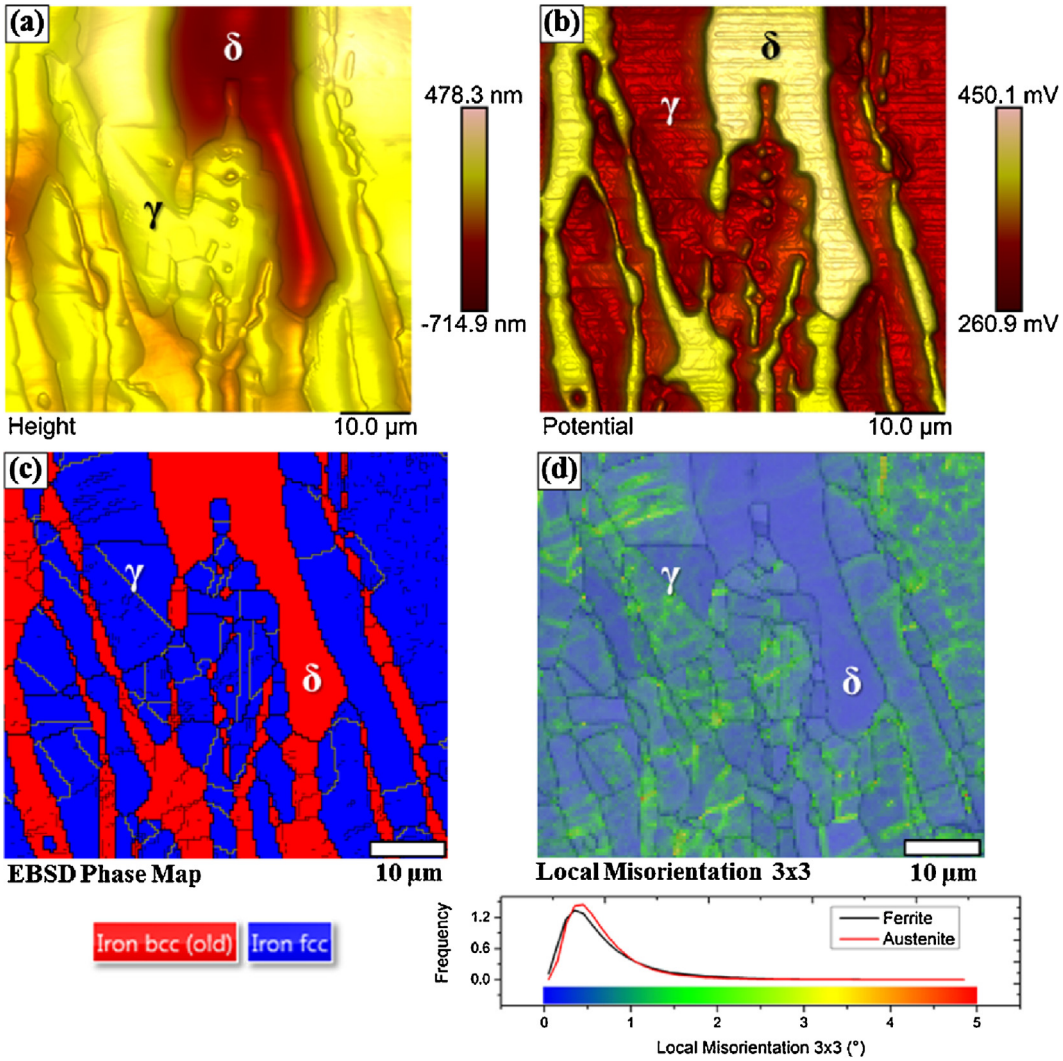

Fig. 2. SKPFM on annealed sample showing (a) surface topography and (b) Volta potential maps at 38% RH, with (c) the corresponding EBSD phase map, and (d) local misorientation map (LMO) indicating the distribution of plastic strain. Thick black lines are HAGB's, thin black lines LAGB's, and yellow lines are twin boundaries (CSL $\Sigma 3$). (For interpretation of the references to colour in this figure legend, the reader is referred to the web version of this article.)

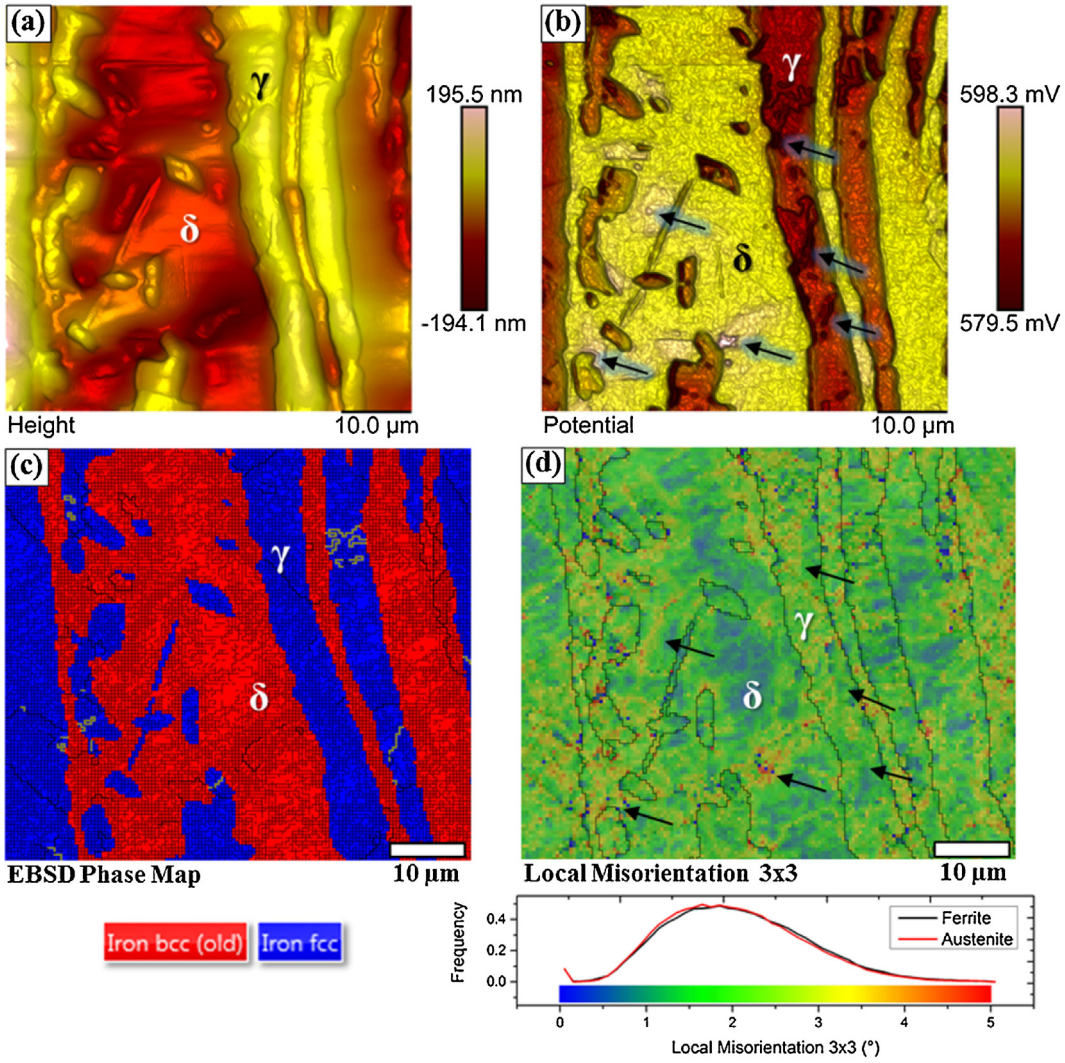

Fig. 3. SKPFM of 40% cold-rolled duplex stainless steel with (a) topography map, (b) Volta potential map at 38% RH, and (c) corresponding EBSD phase map, and (d) LMO map indicating local strain (black lines show phase boundaries). Thick black lines are HAGB's, thin black lines LAGB's, and yellow lines are twin boundaries (CSL Σ3); with the arrows in (b and d) show local potential hot-spots. (For interpretation of the references to colour in this figure legend, the reader is referred to the web version of this article.)

which seemed show to local heterogeneities across the surface [44].

In addition, the $\Delta\Psi$ difference measured between ferrite and austenite decreased to only about 5–10 mV difference, with ferrite assuming Volta potential values of 593 ± 5 mV, whilst austenite showed 589 ± 5 mV. Hence, the driving force for micro-galvanic interaction between both phases is expected to have decreased significantly by cold deformation. However, local ($\Delta\Psi$) potential hot-spots within both phases have become visible which were not present prior to cold work, indicating preferential sites of localised electrochemical activity (arrows in Fig. 3b). There were numerous local hot-spots, indicating enhanced selective net anodic activity in the ferrite with typical ($\Delta\Psi$) values of 598 ± 2 mV. This indicates a higher local electronic activity at these confined regions.

In addition, hot-spots with lower $\Delta\Psi$ were formed in austenite with values of 580 ± 3 mV. Such sites would indicate lower electronic activity i.e., enhanced selective net cathodic behaviour but potential gradients surrounding hot-spot zones can trigger local galvanic activity, hence enhance the surface reactivity at these confined regions and so facilitate preferential electrochemical attack. Large potential gradients at these confined regions, measured over short distances are expected to trigger localised attack in contrast to regions with smaller potential gradients.

In general, large $\Delta\Psi$ gradients can affect the galvanic interaction between individual phases. After cold deformation, the overall potential gradient at the interphases decreased, which indicates a reduction of galvanic interaction between ferrite and austenite. Such sites would still be expected to behave preferentially active, but a selective attack on ferrite only, as observed in the annealed condition, would not be expected. Furthermore, the region over which potential changes occurred in the cold-rolled condition became larger, and sites of local potential gradients (hot-spots) were observed in both phases meaning that both ferrite and austenite would be expected to be electrochemically active, but ferrite obviously more due to the nobler potential. The variation of $\Delta\Psi$ within each crystallographic phase is most likely associated with the presence of dislocation-related strain fields adjacent to interphases, due to the inherent crystallographic mismatch between ferrite and austenite. The EBSD phase map (Fig. 3c) shows LAGB's concentrated in both ferrite and austenite, with highly deformed regions consisting of accumulated LAGB's particularly visible at the interphase (Fig. 3d). The observed SKPFM hot-spots in Fig. 3b

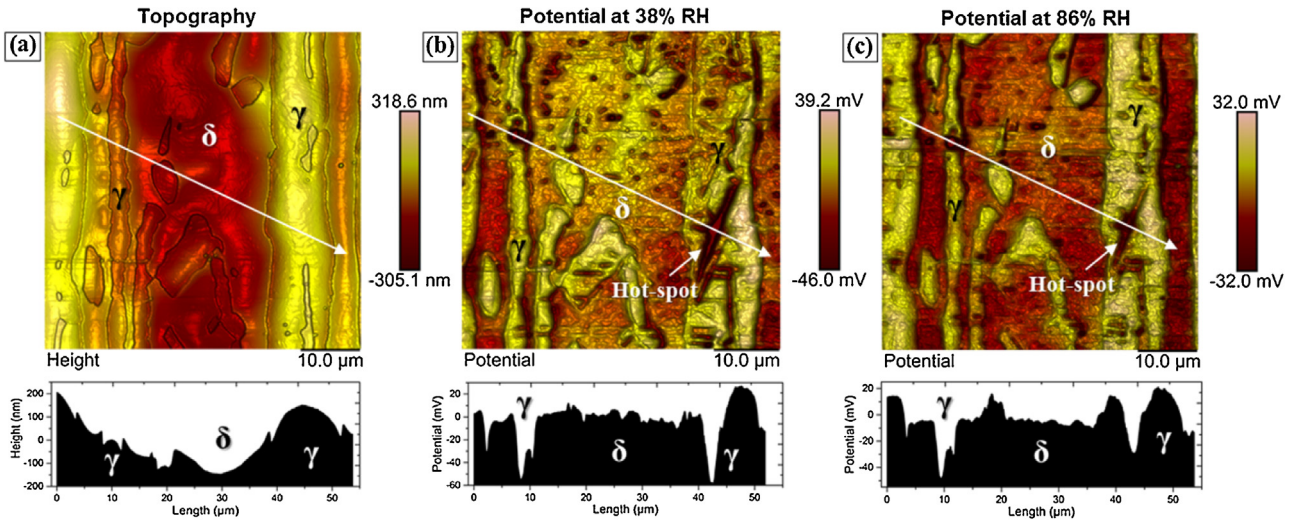

Fig. 4. SKPFM of 40% cold-rolled 2205 duplex stainless steel with (a) topography map, (b) mathematically inverted Volta potential map at 38% RH, and (c) Volta potential map at 86% RH. The inversion of the Volta potential map clearly shows local potential hot-spots. Local potential hot-spots remained in humid environment indicating corrosion-active sites. Potential maps were flattened using 1st order flattening therefore the values are relative only.

seemed to be associated with some of the misorientation hot-spots observed in Fig. 3d. Also, the mean LMO shows a broader distribution with a maximum value of nearly 5°, indicating the presence of large local strain variations in the microstructure. It should be noted that during plastic deformation local chemical variations and surface roughness can be altered, which would also contribute to the measured $\Delta\Psi$.

Further SKPFM analysis was performed in humid air (86% RH) to assess whether the observed local ($\Delta\Psi$) differences at low RH were also present. The surface topography map with corresponding Volta potential maps at 38% RH and 86% RH of the 40% cold-rolled specimen are shown in Fig. 4. Both Volta potential maps were flattened using 1st flattening order and mathematically inverted to obtain an enhanced contrast of local potential hot-spots. The

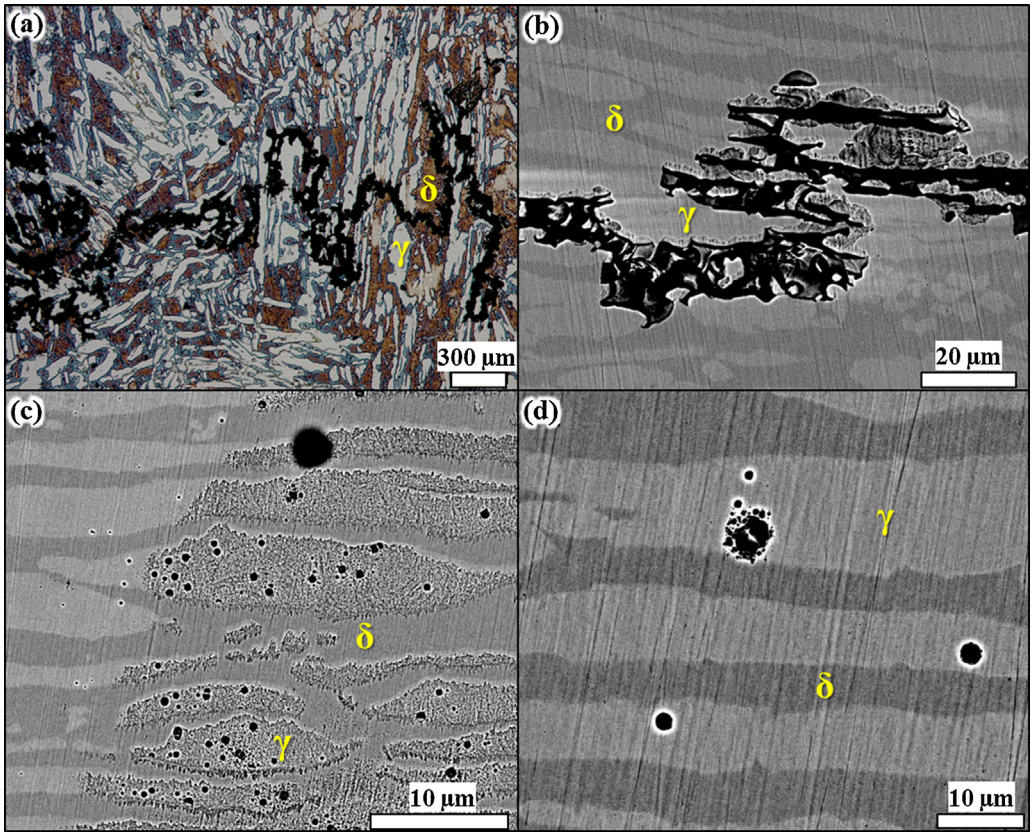

Fig. 5. Corrosion morphology after exposure to atmospheric corrosion with (a) optical micrograph of mill-annealed microstructure showing selective corrosion on ferritic regions (stained) with 290 µg/cm^2 DD of chloride ($MgCl_2$), (b) SEM image showing selective corrosion of ferrite with slight attack occurred on austenite with 2856 µg/cm^2 DD of chloride ($MgCl_2$), and (c and d) SEM images of the 40% cold-rolled microstructure showing numerous pits formed primarily in austenite after exposure to 1450 µg/cm^2 DD of chloride ($MgCl_2$).

latter produces a better contrast but reverses the potential ranking order (i.e., austenite has higher potential difference). Several local $\Delta\Psi$ hot-pots were observed in both the ferrite and austenite, indicating local corrosion-activity. These local potential variations with discrete potential extremes causing potential contrasts indicate micro-galvanic coupling within both phases and at interphase boundaries. Some larger, trench-like regions in austenite are also present, indicating similar ($\Delta\Psi$) differences. These regions are currently subject to further investigations.

In dry air, the passivating layer of stainless steels consists of a thin film oxide/oxyhydroxide layer, usually 1–3 nm [25,46,47]. In humid air above 60% RH, at least ten monolayers of water will be adsorbed resulting in thicker passivating layers which decreases the Volta potential difference [25,48]. It has been reported that this potential drop is in the order of 50–100 mV [48]. However, the measurement in Fig. 4 gives a potential drop of 200 mV in 86% RH compared to 38% RH. Water molecules could have adsorbed onto the Pt probe which may have resulted in a minor change in the Volta potential of the Pt probe.

The corrosion behaviour of the mill-annealed and 40% cold-rolled microstructures after exposure for 212 h to 86% RH atmospheric environment is shown in Fig. 5. The ferrite selectively corrodes in this environment [32–35], supported by observations in Fig. 5(a and b). The corrosion attack showed a filiform-like appearance, percolating through the microstructure. Corrosion initiated on interphase boundaries and propagated preferentially over ferrite regions indicating net anodic behaviour while austenite was the net cathode. Slight attack on some austenite parts, however, has been observed indicating less favoured corrosion attack occurring from the ferrite towards the austenite phase. After cold rolling almost no selective corrosion of the ferrite was observed, but localised corrosion attack occurred at discrete sites primarily located in the austenite (Fig. 5c and d). Local initiation sites of pitting corrosion in austenite were primarily located in the grain interior, possibly related to regions containing local plastic strains. Alternatively, some of these discrete sites may also be associated with strain-induced martensite, which has been reported for duplex stainless steels [49,50].

These observations are in line with data shown in Fig. 3 and Fig. 4, supporting the notion that local microstructure can affect macroscopic corrosion behaviour. The work also highlights how the degradation mechanisms of a material can change as a function of microstructure strain condition. The change from selective corrosion to localised attack could be a potential concern for components with thin wall thickness, and local susceptible sites that follow from cold working may also facilitate stress corrosion crack initiation.

4. Conclusions

1) Volta potential differences of the solution-annealed microstructure measured over austenite and ferrite differed by 70–90 mV, with ferrite indicating a net anodic potential. The latter is expected to facilitate micro-galvanic coupling between ferrite and austenite, resulting in selective dissolution of the ferrite with atmospheric exposure to $MgCl_2$ containing solutions.
2) The introduction of 40% cold-roll reduction significantly reduced the Volta potential difference between ferrite and austenite, but in parallel increased the mean Volta potential difference of the entire microstructure.
3) Volta potential differences maps of the cold-rolled microstructure showed local potential hot-spots (highly active sites at confined regions) with exposure to both 38% and 86% RH environment, indicating corrosion-active sites.
4) After 40% cold rolling, localised pitting corrosion in austenite and only little attack on ferrite was observed, supporting changes to the overall corrosion response of the duplex stainless steel microstructure.

Acknowledgement

The authors acknowledge Radioactive Waste Management (RWM) grant number NPO004411A-EPS02 and EPSRC grant number EP/I036397/1 for financial support. The authors are grateful for the kind provision of Grade 2205 Duplex Stainless Steel plate by Rolled Alloys. The authors also appreciate the valuable comments provided by Dr Robert Winsley, Radioactive Waste Management Ltd. and Dr Anthony Cook, The University of Manchester.

References

[1] C. Fukuoka, K. Morishima, H. Yoshizawa, K. Mino, Misorientation development in grains of tensile strained and crept 2.25%Cr–1%Mo steel, Scr. Mater. 46 (2002) 61–66.
[2] J. Johansson, M. Odén, Load sharing between austenite and ferrite in a duplex stainless steel during cyclic loading, Metall. Mat. Trans. A 31 (2000) 1557–1570.
[3] J.-O. Nilsson, G. Chai, The physical metallurgy of duplex stainless steels. International Conference & Expo DUPLEX, Associazione Italiana Di Metallurgia–AIM, Grado, Italy, 2007.
[4] G.S. Frankel, Pitting corrosion of metals: a review of the critical factors, J. Electrochem. Soci. 145 (1998) 2186–2198.
[5] W. Ozgowicz, A. Kurc-Lisiecka, A. Grajcar, Corrosion behaviour of cold-deformed austenitic alloys, in: M. Aliofkhazraei (Ed.), Resistance to Corrosion and Passivity of 316L Stainless Steel Directionally Solidified Samples, Developments in Corrosion Protection, InTech, 2014, 2015.
[6] T. Prosek, A. Le Gac, D. Thierry, S. Le Manchet, C. Lojewski, A. Fanica, E. Johansson, C. Canderyd, F. Dupoiron, T. Snauwaert, F. Maas, B. Droesbeke, Low-temperature stress corrosion cracking of austenitic and duplex stainless steels under chloride deposits, Corros. Sci. 70 (2014) 1052–1063.
[7] U. Krupp, A. Giertler, M. Söker, H. Fu, B. Dönges, H.J. Christ, K. Istomin, A. Hüsecken, U. Pietsch, C.P. Fritzen, W. Ludwig, Significance and mechanism of the crack initiation process during very high cycle fatigue of duplex stainless steel, Procedia Eng. 74 (2014) 143–146.
[8] G. Kordatos, The effect of cooling rate on the mechanical and corrosion properties of SAF 2205 (UNS 31,803) duplex stainless steel welds, Scri. Mater. 44 (2001) 401–408.
[9] K. Mino, C. Fukuoka, H. Yoshizawa, Evolution of intragranular misorientation during plastic deformation, J. Jpn. Instit. Metals 64 (2000) 50–55.
[10] W. Li, M. Cai, Y. Wang, S. Yu, Influences of tensile strain and strain rate on the electron work function of metals and alloys, Scr. Mater. 54 (2006) 921–924.
[11] D.Y. Li, Electron work function at grain boundary and the corrosion behavior of nanocrystalline metallic materials, MRS Online Proc. Library 887 (2005), 0887-Q05-03.1.
[12] Moore, W. J., Physikalische Chemie. 4. Auflage ed., Walter de Gruyter, 1986.
[13] A. Nazarov, D. Thierry, Application of Volta potential mapping to determine metal surface defects, Electrochim. Acta 52 (2007) 7689–7696.
[14] M. Nonnenmacher, M.P. O'Boyle, H.K. Wickramasinghe, Kelvin probe force microscopy, Appl. Phys. Lett. 58 (1991) 2921–2923.
[15] M. Rohwerder, F. Turcu, High-resolution Kelvin probe microscopy in corrosion science: Scanning Kelvin probe force microscopy (SKPFM) versus classical scanning Kelvin probe (SKP), Electrochim. Acta 53 (2007) 290–299.
[16] V.S. Bagotsky, Fundamentals of Electrochemistry. The Electrochemical Society Series, Wiley-Interscience, Hoboken, New Jersey, 2006.
[17] J.O.M. Bockris, A.K.N. Reddy, M. Gamboa-Aldeco, Modern Electrochemistry 2A. Fundamentals of Electrodics, vol. 2A, Kluwer Academic Publishers, New York, 2002, pp. 1–817.
[18] G.S. Frankel, V. Guillaumin, P. Schmutz, Characterization of corrosion interfaces by the scanning Kelvin probe force microscopy technique, J. Electrochem. Soc. 148 (2001) B163–B173.
[19] S. Sadewasser, T. Glatzel, Kelvin Probe Force Microscopy Measuring and Compensating Microscopy, Springer, Heidelberg, 2012.
[20] W. Li, D.Y. Li, Effect of surface geometrical configurations induced by microcracks on the electron work function, Acta Mater. 53 (2005) 3871–3878.
[21] W. Li, D.Y. Li, Variations of work function and corrosion behaviors of deformed copper surfaces, Appl. Surf. Sci. 240 (2005) 388–395.
[22] W. Li, D.Y. Li, Influence of surface morphology on corrosion and electronic behavior, Acta Mater. 54 (2006) 445–452.
[23] A.B. Cook, Z. Barrett, S.B. Lyon, H.N. McMurray, J. Walton, G. Williams, Calibration of the scanning Kelvin probe force microscope under controlled environmental conditions, Electrochim. Acta 66 (2012) 100–105.
[24] S. Yee, R.A. Oriani, M. Stratmann, Application of a Kelvin microprobe to the corrosion of metals in humid atmospheres, J. Electrochem. Soc. 138 (1991) 55–61.

[25] C. Leygraf, T.E. Graedel, Atmospheric Corrosion, John Wiley & Sons, Canada, 2000.
[26] T.D. Hicks, P.J. Baldwin, P.J. Hooker, N.A. Richardson, I.G. Chapman, Concepts for the Geological Disposal of Intermediate-level Radioactive Waste, Galson Sciences Ltd., Oakham, Rutland, UK, 2008.
[27] R.V. Lapshin, Automatic lateral calibration of tunneling microscope scanners, Rev. Sci. Instrum. 69 (1998) 3268–3276.
[28] IASTM International, ASTM A 923–Standard Test Methods for Detecting Detrimental Intermetallic Phase in Duplex Austenitic/Ferritic Stainless Steels, ASTM International, West Conshohocken, PA, 2003.
[29] J.Y. Choi, J.H. Ji, S.W. Hwang, K.-T. Park, Strain induced martensitic transformation of Fe–20Cr–5Mn–0.2Ni duplex stainless steel during cold rolling: effects of nitrogen addition, Mater. Sci. Eng.: A 528 (2011) 6012–6019.
[30] N. Sathirachinda, R. Pettersson, J. Pan, Depletion effects at phase boundaries in in 2205 duplex stainless steel characterized with SKPFM and TEM/EDS, Corros. Sci. 51 (2009) 1850–1860.
[31] M. Femenia, J. Pan, C. Leygraf, Characterization of ferrite-austenite boundary region of duplex stainless steels by SAES, J. Electrochem. Soc. 151 (2004) B581–B585.
[32] C. Örnek, A.H. Ahmed, D.L. Engelberg, Effect of microstructure on atmospheric-induced corrosion of heat-treated grade 2205 and 2507 duplex stainless steels, in: Eurocorr, Dechema, Istanbul, Turkey, 2012, pp. 1–10.
[33] C. Örnek, D.L. Engelberg, Effect of 475(C embrittlement on the corrosion behaviour of grade 2205 duplex stainless steel investigated using local probing techniques, in: Corrosion Management, The Institute of Corrosion, Northampton, UK, 2013, pp. 9–11.
[34] C. Örnek, D.L. Engelberg, Kelvin probe force microscopy and atmospheric corrosion of cold-rolled grade 2205 duplex stainless steel, in: Eurocorr, European Federation of Corrosion, Pisa, Italy, 2014, pp. 1–10.
[35] D.L. Engelberg, C. Örnek, Probing propensity of grade 2205 duplex stainless steel towards atmospheric chloride-induced stress corrosion cracking, Corros. Eng. Sci. Technol. 49 (2014) 535–539.
[36] A.M. do Nascimento, M.C.F. Ierardi, A.Y. Kina, S.S.M. Tavares, Pitting corrosion resistance of cast duplex stainless steels in 3.5% NaCl solution, Mater. Charact. 59 (2008) 1736–1740.
[37] M. Femenia, J. Pan, C. Leygraf, P. Luukkonen, In situ study of selective dissolution of duplex stainless steel 2205 by electrochemical scanning tunnelling microscopy, Corros. Sci. 43 (2001) 1939–1951.
[38] K. Aoki, H. Ito, M. Miyasaka, J. i. Sakai, Potential dependence of preferential dissolution behavior of a duplex stainless steel in simulated solution inside crevice, Zairyo-to-Kankyo 60 (2011) 363–367.
[39] H. Aoki, K. Mitsuhashi, J. i. Sakai, Dissolution behavior of α and γ phases of a duplex stainless steel in a simulated crevice solution, ECS Trans. 25 (2010) 17–22.
[40] R.A. Cottis, R.C. Newman, Stress corrosion cracking resistance of duplex stainless steels, Health Saf. Executive (1993) 58.
[41] B. Cottis, M. Graham, R. Lindsay, S. Lyon, T. Richardson, D. Scantlebury, H. Stott, in: B. Cottis, M. Graham, R. Lindsay, S. Lyon, T. Richardson, D. Scantlebury, H. Stott (Eds.), Shreir's Corrosion–Volume 2, vol. 1, Elsevier B.V., Manchester, 2010.
[42] C.-M. Tseng, W.-T. Tsai, H.-Y. Liou, Effect of nitrogen content on the environmentally-assisted cracking susceptibility of duplex stainless steels, Metall. Mat. Trans. A 34 (2003) 95–103.
[43] J.-S. Lee, K. Fushimi, T. Nakanishi, Y. Hasegawa, Y.-S. Park, Corrosion behaviour of ferrite and austenite phases on super duplex stainless steel in a modified green-death solution, Corros. Sci. (2014).
[44] R. Hausbrand, M. Stratmann, M. Rohwerder, The physical meaning of electrode potentials at metal surfaces and polymer/metal interfaces: consequences for delamination, J. Electrochem. Soc. 155 (2008) C369–C379.
[45] A.S. Hamada, L.P. Karjalainen, M.C. Somani, Electrochemical corrosion behaviour of a novel submicron-grained austenitic stainless steel in an acidic NaCl solution, Mater. Sci. Eng.: A 431 (2006) 211–217.
[46] T.E. Graedel, R.P. Frankenthal, Corrosion mechanisms for iron and low alloy steels exposed to the atmosphere, J. Electrochem. Soc. 137 (1990) 2385–2394.
[47] S.D. Cramer, B.S. Covino, ASM Handbook, Volume 13A: Corrosion: Fundamentals, Testing, and Protection. vol. 13, ASM Int. (2003).
[48] P. Marcus, F. Mansfeld, Analytical Methods in Corrosion Science and Engineering, Taylor & Francis Group, Boca Raton, FL, USA, 2006.
[49] L.W. Tsay, M.C. Young, C.S. Shin, S.L.I. Chan, Hydrogen-enhanced cracking of 2205 duplex stainless steel, Fatigue Fract. Eng. Mater. Struct. 30 (2007) 1228–1236.
[50] Y. Guo, J. Hu, J. Li, L. Jiang, T. Liu, Y. Wu, Effect of annealing temperature on the mechanical and corrosion behavior of a newly developed novel lean duplex stainless steel, Materials 7 (2014) 6604–6619.